Nano Letters 19.12 (2019): 8597-8604

DOI: https://doi.org/10.1021/acs.nanolett.9b03153

Three-dimensional superconducting nano-helices grown by He^+-focused-ion-beam direct writing

Rosa Córdoba[1,2,3], Dominique Mailly[4], Roman O. Rezaev[5, 6], Ekaterina I. Smirnova[5], Oliver G. Schmidt[5,7], Vladimir M. Fomin[5,8], Uli Zeitler[9], Isabel Guillamón[10], Hermann Suderow[10], and José María De Teresa[1,2,11*]*

[1] *Instituto de Ciencia de Materiales de Aragón (ICMA), Universidad de Zaragoza-CSIC, E-50009 Zaragoza, Spain*

[2] *Departamento de Física de la Materia Condensada, Universidad de Zaragoza, E-50009 Zaragoza, Spain*

[3] *Instituto de Ciencia Molecular, Universitat de València, Catedrático José Beltrán 2, 46980 Paterna, Spain*

[4] *Centre de Nanosciences et de Nanotechnologies, CNRS, Univ Paris Sud, Université Paris Saclay, 91120 Palaiseau, France*

[5] *Institute for Integrative Nanosciences, Leibniz IFW Dresden, Helmholtzstraße 20, D-01069 Dresden, Germany*

[6] *Tomsk Polytechnic University, Lenin Ave. 30, 634050 Tomsk, Russia*

[7] *Research Center for Materials, Architectures and Integration of Nanomembranes (MAIN), Rosenbergstraße 6, TU Chemnitz, D-09126 Chemnitz, Germany*

[8] *National Research Nuclear University MEPhI (Moscow Engineering Physics Institute), Kashirskoe shosse 31, 115409 Moscow, Russia*

[9]*High Field Magnet Laboratory (HFML-EFML), Radboud University, Nijmegen, 6525 ED Nijmegen, The Netherlands*

[10]*Laboratorio de Bajas Temperaturas y Altos Campos Magnéticos, Departamento de Física de la Materia Condensada, Instituto de Ciencia de Materiales Nicolás Cabrera, Condensed Matter Physics Center (IFIMAC), Universidad Autónoma de Madrid, 28049, Madrid, Spain*

[11] *Laboratorio de Microscopías Avanzadas (LMA)-Instituto de Nanociencia de Aragón (INA), Universidad de Zaragoza, E-50018 Zaragoza, Spain*

Table of contents graphic

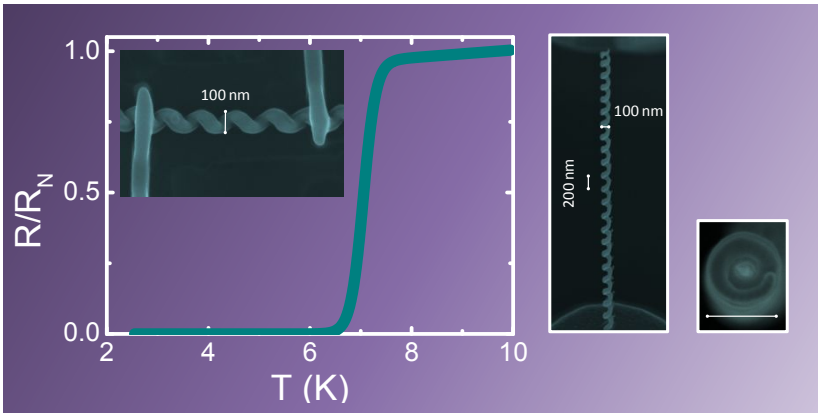

ABSTRACT 150–250 words

Novel schemes based on the design of complex three-dimensional nanoscale architectures are required for the development of the next generation of advanced electronic components. He^+

focused-ion-beam (FIB)-microscopy in combination with a precursor gas allows to fabricate three-dimensional nanostructures with an extreme resolution, and a considerably higher aspect ratio than FIB-based methods, such as Ga^+ FIB induced deposition, or other additive manufacturing technologies. In this work, we report the fabrication of three-dimensional tungsten carbide (WC) nano-helices with on-demand geometries via controlling key deposition parameters. Our results show the smallest and more-densely-packed nano-helix ever fabricated so far, with dimensions of 100 nm in diameter, and aspect ratio up to 65. These nano-helices become superconducting at 7 K and show large critical magnetic field and critical current density. In addition, given its helical three-dimensional geometry, fingerprints of vortex and phase-slip patterns are experimentally identified and supported by numerical simulations based on the time-dependent Ginzburg-Landau equation. These results can be understood by the helical geometry that induces specific superconducting properties and paves the way for future electronic components, such as sensors, energy storage elements and nano-antennas, based on three-dimensional compact nano-superconductors.

KEYWORDS

Helium ion microscope, 3D nanoprinting, focused ion beam induced deposition (FIBID), nano-superconductors, phase slips, Ginzburg-Landau equations

TEXT

Superconductors are integrated in major equipment and machinery, for instance as part of powerful magnets [1], employed for nuclear magnetic resonance [2], fusion reactors [3] and particle accelerators [4]. Moreover, they have become excellent materials for energy storage [5], electrical

generators [6], magnetic sensors [7], and high-frequency filters and switches [8,9]. These superconductors normally need nano-engineering to achieve the required performance in those applications[10]. Besides, nanostructured superconductors are central elements in refined quantum computing architectures such as one-dimensional nanowire- based quantum oscillators [11] and highly-integrated Josephson junction networks [12]. From a basic research point of view, superconducting nanostructures are fascinating objects to study vortex confinement caused by defects, geometry and/or topology to preserve the dissipation-free energy state [13,14].

Innovative schemes have taken advantage of the third dimension (3D) for the development of high-performance and energy-efficient electronic components [15]. Thus, 3D nano-superconductivity could represent a breakthrough for future electronics components, particularly for sensors, energy-storage components and quantum computing. A significant improvement of the microwave radiation detection has been demonstrated through the fabrication of a superconducting bolometer by folding 2D superconductor structures into 3D helical belts [16]. However until now, few works of real three-dimensional (3D) superconducting nanostructures have been reported [17–21], mainly because their fabrication and characterization are still challenging.

In the last decades, Ga^+ Focused Ion Beam Induced Deposition (FIBID) has been used to grow functional 3D materials [22–27]. Particularly, 3D superconducting W-based nanowires, with superconducting critical temperature (T_c)~ 5 K and upper critical magnetic field $\mu_0 H_{c2}(0)$~ 9.5 T [17–19], and NbC nanowires with $T_c \approx$ 11 K, were recently grown using respectively $W(CO)_6$ and $Nb(NMe_2)_3(N\text{-}t\text{-}Bu)$ precursor materials. Nevertheless, the resolution in this process is mainly limited by the Ga^+ beam diameter (~5 nm) and its high lateral scattering. This prevents the growth of sub-100 nm 3D nanostructures.

A recent generation of focused particle beam for 3D nano-prototyping is the Helium Ion Microscope (HIM) [28], based on He^+ gas-FIB source with a probe size as small as ≈ 0.3 nm. Thus, HIM represents an enormous step forward for 3D nanoprinting due to the small beam diameter and low proximity effect [29], creating vertical pillars of PtC and WC with diameters down to 40 nm [30,31]. In a recent study, some of the authors have reported on the fabrication of 3D superconducting hollow nanowires as small as 32 nm in diameter, with a T_c≈ 6.4 K, large critical magnetic field and current density [20], opening a new path for the fabrication of more complex 3D nano-objects that could be implemented as future components in electronics.

In this work, we present the fabrication of 3D WC superconducting nano-helices on demand by using a HIM. The nano-helices geometry is successfully controlled with pitches (L_T) between 200 nm and 2.3 μm, nano-helix diameters (D_{NH}) from 100 nm to 295 nm, and nanowire diameter (D_{NW}) as small as 45 nm. These 3D nano-helices display superconductivity below 7 K (T_c), as well as high upper critical magnetic fields $\mu_0 H_{c2}$≈ 15 T, and large critical current densities J_c≈ 0.2 MA/cm^2. The magnetotransport properties at low temperature and under magnetic fields show characteristic features of vortex and phase slip patterns associated with the nano-helix topology and 3D geometry. These experimental data are in good agreement with numerical simulations based on the time-dependent Ginzburg-Landau equation.

We use a HIM focused to ~1 nm in combination with a $W(CO)_6$ precursor to grow individual and vertical 3D WC nano-helices. The precursor flux is delivered into the process chamber and adsorbs to the substrate's surface, whereas the He^+ FIB spot describes a circular shape with a proper overlapping between two consecutive spots and a beam dwell time that favors continuous growth along the third dimension. By keeping the optimized beam parameters, a nano-helix is fabricated increasing the number of turns of the circular shape pattern, as

depicted in the sketch and in the SEM image of a representative nano-helix (deposition parameters: $I_{beam} \approx 1$ pA, beam spacing= 10 nm, nominal diameter= 75 nm, beam dwell time= 700 ms, turns= 23) shown in Figure 1.

To find the optimal parameters for the fabrication of 3D nano-helices, we investigate the resolution limits and dimensional control by varying the diameter and beam dwell time. A linear dependence of the pitch as a function of the beam dwell time for nominal diameters ranging from 75 nm to 200 nm has been found (see Figure S1, Table S1 and Figure S2). The use of such enables us to fabricate 3D helical nanostructures on demand, as shown in Figure 2. The specific deposition parameters and real dimensions of nano-helices from type 1 to type 8 are listed in Table 1. Particularly, nano-helices from type 1 to 5 were grown by keeping fixed the nominal circular diameter to 75 nm and varying the beam dwell time from 700 ms to 2400 ms. Using these parameters, the achieved nano-helix diameter ranges from 100 nm to 146 nm, and the pitch from 200 nm to 1 μm. Nano-helix type 1 is the smallest and more-densely-packed nano-helix ever fabricated so far, with 100 nm in diameter, 200 nm of pitch and 23 turns. Nano-helices from type 6 to 8 were grown by keeping fixed the nominal circular diameter to 200 nm and varying the beam dwell time from 650 ms to 2000 ms. By using these parameters, the nano-helix diameters range from 277 nm to 295 nm, and pitches from 430 nm to 2.3 μm. Further highlights of the fabrication procedure include the very small nanowire diameter of 45 nm and the short process time of only a few minutes. More details regarding growth conditions are described in the Supplementary information (methods section).

For magnetotransport measurements, the 3D nano-helices were placed flat on the SiO_2 layer of a Si/SiO_2 substrate by means of a nanomanipulator. This step is challenging due to the elastic behavior of the nano-helices (see movie in the Supplementary information for

details). Then, four Pt FIBID contacts were grown to connect the nano-helices to pre-patterned Ti pads. Finally, four-probe electrical measurements at low temperature (from 300 K to 0.5 K) and under perpendicularly applied magnetic field to the substrate plane (from 0 T to 9 T) were performed (see Figure S3 and Supplementary information for details of deposition parameters). This process was performed for nano-helices of type 1, 4, 6 and 7 (see Figure 2 and Table 1). On the one hand, we have studied small, both densely-packed and sparsely-packed nano-helices i.e. nano-helix type 1 and 4 with D_{NH}~ 100 nm and D_{NW}~ 50 nm, with a pitch of 200 nm for type 1 and 550 nm for type 4. On the other hand, large and, both densely-packed and sparsely-packed nano-helices were also investigated. These are nano-helices of type 6 and 7 with D_{NH}~ 280 nm and D_{NW}~ 58 nm, with a pitch of 430 nm for type 6 and 925 nm for type 7.

Nano-helices show resistance drops from the normal to the superconducting state at T_c ($0.5R_N$) values between 6.23 K and 7.06 K (see Figure 3(a) and Table 2). Figure 3(b) shows their upper critical magnetic field μ_0H_{c2} (0.9 R_N) as a function of temperature. μ_0H_{c2} is extracted from the resistance versus temperature curves under perpendicular magnetic field (i.e. inset of Figure 3(b)). We fit $\mu_0H_{c2}(T)$ to a simple power law equation $\mu_0 H_{c2}(T) \propto \left(1 - T/T_c\right)^n$. For a 2D film and a perpendicular magnetic field or a 3D bulk sample, we expect usual Werthammer-Helfand-Hohenberg behavior [32], with n~ 1. For a 1D wire, we expect n=0.5 [14]. Here we find n in between, ranging from 0.72 to 0.78 for nano-helices with a nanowire diameter between 50 nm and 58 nm, respectively. The deviation from the usual 1D and 3D behaviors suggests that nano-helices have an intermediate superconducting behavior [33]. Moreover, we find that μ_0H_{c2}(0 K) ranges from 12.1 T to 15.3 T in different helices. Using the orbital limit estimation of $\mu_0 H_{c2}(T) = \Phi_0/2\pi\xi^2(T)$, the Cooper pair coherence length, ξ, at 0 K is found to range from 4.64 to 5.22 nm. Considering nano-helices as type II superconductors in the weak coupling regime and in the dirty limit, the magnetic field

penetration length (λ) can be estimated applying the following expression $\lambda(0) = 1.05 \times 10^{-3}\sqrt{\rho_N/T_c}$ derived from the Gor'kov theory [34]. λ values range from 603 nm to 733 nm.

The highest value of J_c (0.5 K, 0 T) ~ 0.23 MA/cm^2 is found for the smallest and more-densely-packed nano-helix (type 1), which is twice higher than the value for sparsely-packed nano-helices (type 6 and 7) (see Figure S4 in the Supplementary information). J_c values are around 80 times lower than the depairing current density[35], J_d (0.5 K, 0 T) ~ 17.8 MA/cm^2 (see Table 2), at which the electromagnetic energy due to the current flow is equal to the superconducting condensation energy. Such a difference is found almost invariably in all superconductors indicating that dissipation sets in well below the depairing energy due to formation of phase slips or vortices significantly below the depairing current. Besides, sample inhomogeneities, such as grain boundaries, differences in composition, nano-defects or amorphisation over these small dimensions can produce a depression effect on the critical current density of the nano-helices. To conclude, the calculated superconducting parameters of 3D nano-helices are comparable with those found in He^+ FIBID out-of-plane hollow nanowires[20], and He^+ FIBID in-plane nanowires used in hybrid microwave resonators[36]. The kinetic inductance for this material is ~ 15 pH/□, which is 250 times higher than the geometrical inductance[36], making them good candidates for the fabrication of highly-packed 3D nano-resonators.

We have observed an enhancement of the free-dissipation ground state, $\mu_0 H_{min}$ (defined as the field value at which resistance reach $0.1R_N$) for the nano-helix type 7 (Figure 4(a)). It is 35 % larger compared to hollow nanowires grown by He^+ FIBID [20]. This suggests that the helix provides much stronger pinning as compared to straight nanowires [37]. We will develop this in detail below, but we point out that such an improvement can be used to build better superconducting logic gates [38], quantum switches [39] and single-photon detectors [40–42].

On the other hand, the dependence of $\mu_0 H_{c2}$ for the nano-helix when tilting the magnetic field is not large, but finite (Figure 4(b)). This suggests that the direction of the magnetic field, compared to the precise geometry, plays a significant role in the upper critical field (we discuss this in more detail in the Supplementary Information).

An interesting feature only visible in resistance-versus-current measurements for the nano-helix type 6 is that the resistive transition occurs in various steps, as observed in measurements under fixed perpendicular magnetic field of 1 T and 2 T (see Figure 5). Nano-helices type 1, 4 and 7 do not show this feature (see Figure S5). In order to provide some insight to this behavior, numerical simulations based on the time-dependent Ginzburg-Landau equation coupled with Poisson equation have been solved by finite-difference time-domain method (see Supplementary Information, numerical simulations). This analysis reveals several patterns of the order parameter corresponding to the spatial distribution of the normal to the surface component of the magnetic field over the surface of the helical nanostructure. These patterns are represented in the right panels of Figure 5(a) and (b) for magnetic fields 1 T and 2 T, respectively. The order parameter distribution over the surface of the helical structure is shown at different values of the applied transport current (in units of the critical current). The voltage generated by an individual vortex in motion for all patterns leads to a finite resistance of the order of 1 Ω. Experimentally observed jumps (higher than 100 Ω) in the Resistance vs Current charactertistics are about two orders of magnitude higher than the resistance induced by an individual vortex, which follows from our numerical simulation (see Supplementary Information). The most probable reason for the observed jumps is therefore the occurrence of *phase slips*, which start to appear at transport current values shown in Figure 5. The transition of *two* half-turns into the full phase-slip regime causes the resistance to increase by about 1000 Ω, whereas the presence of the phase slip in *all* half-turns without the vortex dynamics results in a resistance of about 2250 Ω. The

simulated order parameter at a magnetic field B = 1 T shown in Figure 5(a) does not seem to reveal vortices in static or dynamic states. From an arbitrary initial state (for which a random distribution was taken), the order parameter evolves to one of the three following quasi-stationary patterns: (i) pure vortex state (the amount of vortices is in the range from 0 to N), (ii) mixed one – vortices plus order parameter depression regions (phase slip) and (iii) pure order parameter depression regimes. We suggest that the whole half turn, at which the order parameter depression appears, switches to the normal state due to the Joule heating as shown in Figures S6. In regions where the absolute value of the normal to surface magnetic field is minimal, the order parameter depression extent is suppressed. This mechanism explains the experimental step-like resistance vs current dependence. Our numerical simulations are described in the Supplementary information (numerical simulations section, inputs from Tables S2 and S3. As distinct from the planar 2D superconductor structures, the complex 3D geometry of nano-helices determines topologically non-trivial screening currents and confinement potentials that cardinally depend on radius and pitch (or, equivalently, curvature and torsion) and imply, as shown below, occurrence of different patterns of topological defects. For all structures, we have observed similar behavior when the applied current increases from 0 to the critical value: *the modulus of the order parameter evolves from a homogeneous state, which describes the pure superconducting phase, to different patterns of vortices, then to different phase-slip patterns, finally resulting in the normal state.* We have found that a phase-slip pattern itself may depend on the number of turns. In order to check how phase-slip patterns evolve with increasing number of turns, we have performed a simulation for structures with fixed width (50 nm), helical diameter (100 nm), and pitch (200 nm) under a magnetic field of 2 T. These geometrical characteristics of the simulated structures correspond to the experimental helix type 1. Results of this simulation for fixed applied transport current ($I \sim 0.6I_c$) are shown in Figure S7. For the structure with one turn,

phase slips are represented by three extended regions over the half-turns. Phase slips occupy approximately 80 % of the area of the structure. For the structure with two turns, there are 5 regions with phase slips, while the relative size of each phase slip region being smaller than the relative size of a phase-slip region for the structure with one turn. The trend of decreasing the size of the phase-slip regions and increasing their number continues for the structure with three turns. For the structure with four turns, the phase-slip regions disappear in some parts of the structure. The increment of the resistance is proportional to the overall size of the phase-slip regions, so, when the phase-slip pattern is represented by a number of small regions, each new region gives a small increment to the resistance (the case realized in helix types 1, 4, 7). In this case, there will occur no shelf-like features in the Resistance-vs-Current dependence within the experimental conditions. Figures S7, S8 and S9 demonstrate how chirality of the nano-helices determines the order-parameter patterns that are quite distinct from those in the planar structures and thus provide an insight into the occurrence of the shelf-like features in the Resistance-vs-Current characteristics in some nano-helices, while there are no such features in other nano-helices.

Despite the overall superconducting properties (T_c, H_{c2}, J_c) of all nano-helices are similar given the same composition, their behaviour is different in various cases, because the complex 3D geometry of a nano-helix leads to disconnected screening currents and richly diversified confinement potentials that shape drastically different patterns of vortices (see, e.g., different multiple disconnected vortex arrays in nano-helices with different numbers of windings [37]) and phase slips (see Figure S7).

To conclude, we report a direct-write methodology to fabricate 3D superconducting nano-helices on demand by using $W(CO)_6$ precursor with a highly-focused He^+ beam. The resulting 3D nano-helices have diameters as small as 100 nm and pitches down to 200 nm, making them the smallest and more-highly-dense packed nano-helices ever grown, which is

unachievable with other manufacturing techniques. By studying their magnetotransport properties, we have found that they exhibit superconducting properties below T_c= 7 K, as well as high critical magnetic field and critical current density. Moreover, signatures of vortex and phase-slip patterns due to their helical three-dimensional geometries are experimentally found. This behavior is attributed to the specific order parameter and magnetic field distributions, which favors the formation of superconducting vortices and order parameter depressions (phase slips) in given regions, as supported by our numerical simulations. Our methodology represents an accurate and reproducible bottom-up approach for the fabrication of innovative, better performance and more compact 3D nano-architectures (Figure S12).

FIGURES

Figure 1. Left: sketch of the growth of 3D nano-helix by He^+-FIBID. Right: SEM image of a WC 3D nano-helix type 1, in which pattern parameters are indicated, D_{NW}= nanowire diameter, D_{NH}= nano-helix diameter, L_T= turn length/pitch, L_{NH}= nano-helix length (52º tilted stage). The specific deposition parameters for the helix shown are: I_{beam}≈ 1 pA, beam spacing= 10 nm, nominal diameter = 75 nm, beam dwell time= 700 ms, turns= 23.

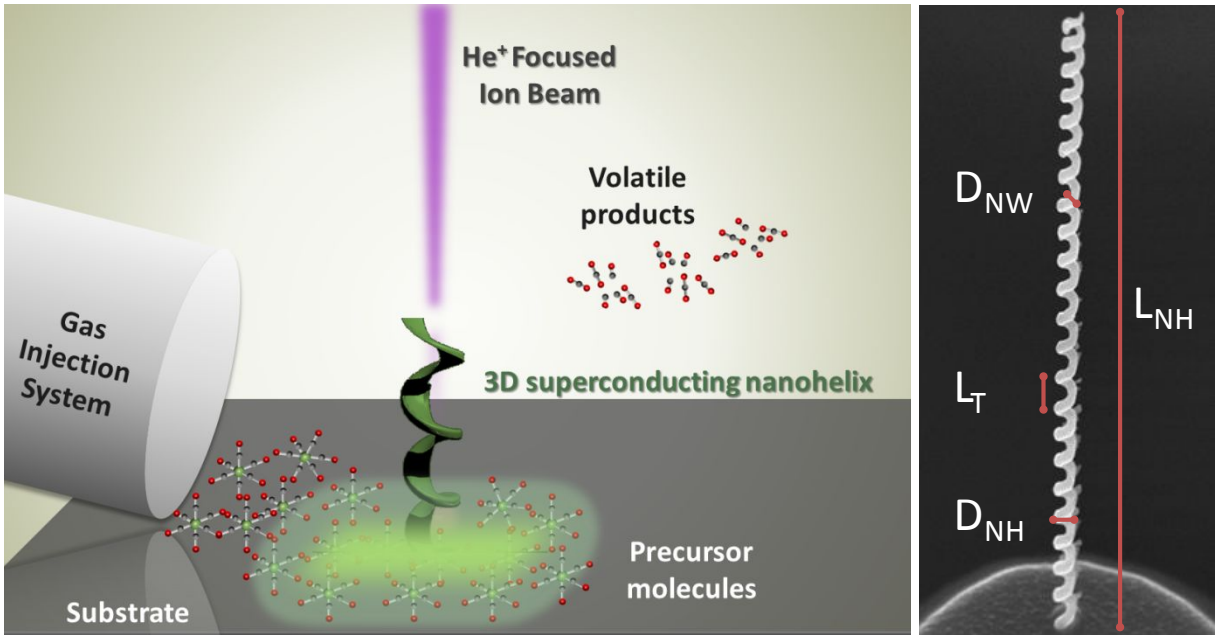

Figure 2. SEM images of WC nano-helices of several types (from 1 to 8) grown by He^{+}-FIBID (52º tilted stage). ΔV represents the locations of the voltage contacts. Inset in the SEM image type 1 shows the top view of the nano-helix (measured bar= 100 nm).

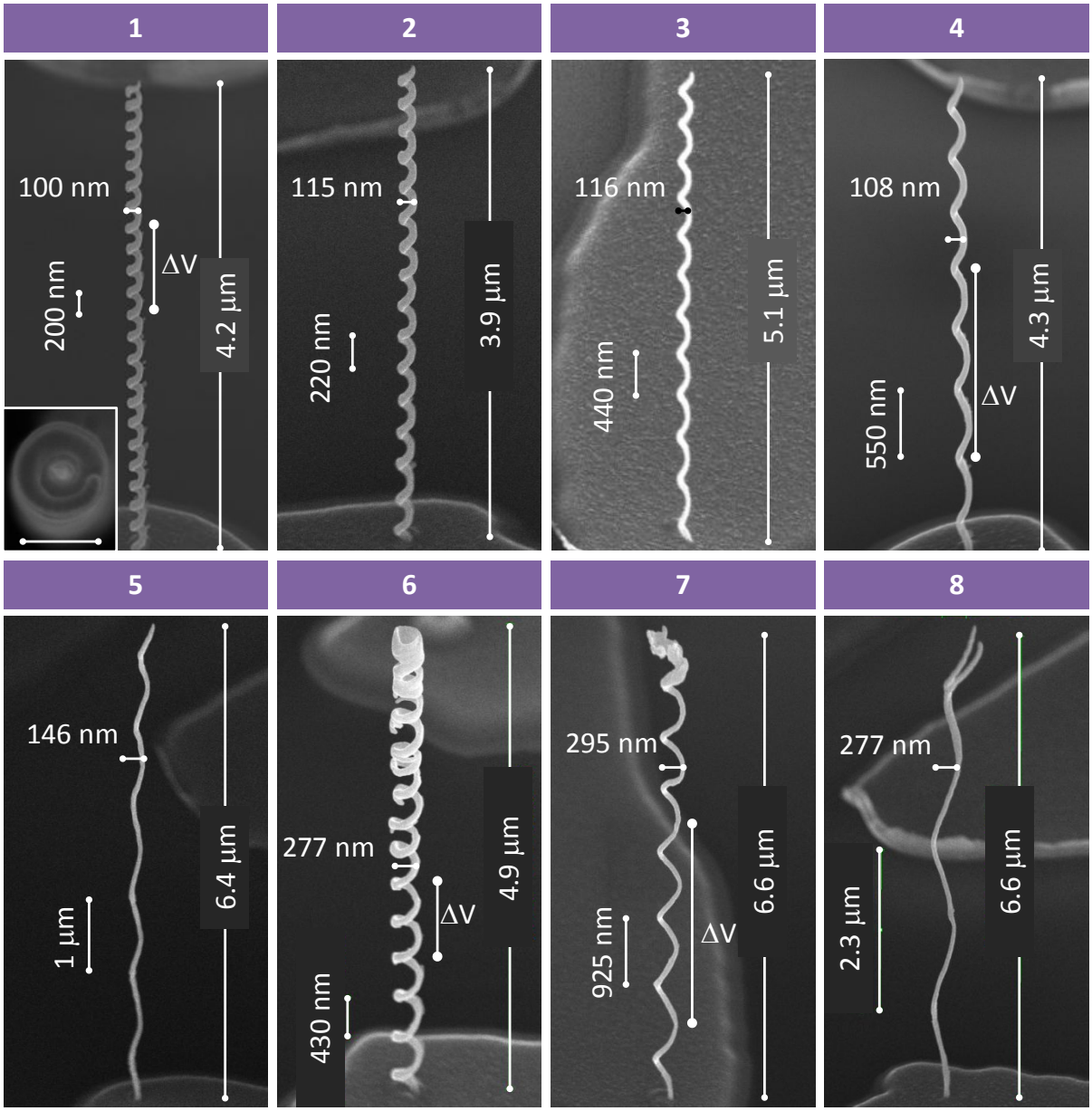

Table 1. Growth parameters, nominal and real dimensions of WC nano-helices shown in Figure 1. For a helix parametrized through the radius R and pitch ($2\pi b$), $x(t) = R\sin t, y(t) = R\cos t, z(t) = bt$, the curvature k_1 and torsion k_2 provide an equivalent representation[43]: $k_1 = \frac{R}{R^2 + b^2}$ and $k_2 = \frac{b}{R^2 + b^2}$. We have selected the "radius-pitch" representation since these parameters directly correlate with the crucial physical parameters of the same dimensionality: coherence length and penetration depth.

Nano-helix nº	**1**	2	3	**4**	5	**6**	**7**	8
Ion current	**0.96**	0.92	0.92	**0.86**	1.47	**1.23**	**1.32**	1.31
Nominal nano-helix diameter (nm)	**75**	75	75	**75**	75	**200**	**200**	200
Repeats	**23**	16	12	**8**	6	**15**	**8**	4
Dwell time (ms)	**700**	1000	1400	**1800**	2400	**650**	**950**	2000
Real nano-helix diameter, D_{NH} (nm)	**100**	115	116	**108**	146	**277**	**295**	277
Nanowire diameter, D_{NW} (nm)	**50**	58	50	**51**	58	**58**	**58**	45
Pitch, L_T (nm)	**200**	220	440	**550**	1000	**430**	**925**	2300
Curvature ($nm^{-1} \times 10^{-3}$)	**14.2**	12.7	7	**5.1**	2.4	**5.8**	**3.4**	0.9
Torsion ($nm^{-1} \times 10^{-3}$)	**9.1**	7.7	8.5	**8.3**	5.2	**2.9**	**3.4**	2.4

Figure 3. (a) Normalized resistance for nano-helices of types indicated in the legend as a function of temperature at 0 T. R_N is the resistance at the normal state, at T=10 K. Inset shows resistance versus temperature for nano-helix type 7. I_{bias}= 100 nA. (b) Upper critical magnetic field ($\mu_0 H_{c2}$) as a function of temperature for nano-helices of types indicated in the legend. Data is fitted to a power low equation. Inset shows resistance as a function of temperature for nano-helix type 7 under perpendicular magnetic field, from 0 to 9 T.

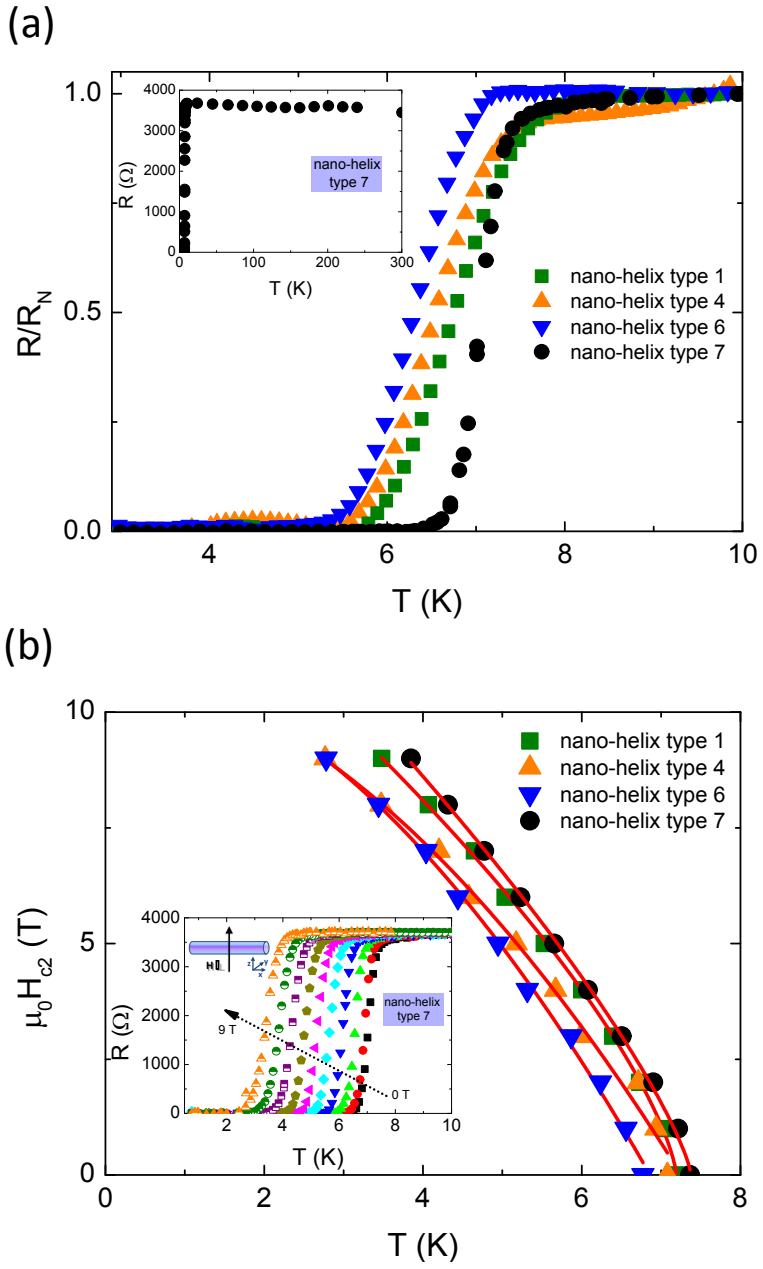

Table 2. Superconducting parameters of nano-helices of types 1, 4, 6 and 7 estimated from experimental magnetotransport measurements.

nano-helix nº	1	4	**6**	**7**
R_N (Ω)	1281	1936	**1796**	**3672**
Number of turns	4	3	**2**	**3**
T_c (K)	6.73	6.50	**6.23**	**7.06**
$\mu_0 H_{c2}$ (0 K) (T)	14.3	12.1	**12.8**	**15.3**
n	0.72 ± **0.01**	0.72 ± **0.04**	**0.76 ± 0.02**	**0.78 ± 0.02**
ξ_0 (nm)	4.80	5.22	**5.07**	**4.64**
λ (nm)	603	629	**733**	**695**
J_c (0.5 K, 0 T) (MA/cm^2)	0.23	0.17	**0.09**	**0.11**
J_d (0.5 K, 0 T) (MA/cm^2)	17.8	15.3	10.8	14.1

Figure 4. (a) Critical magnetic fields as a function of temperature for nano-helix type 7. $\mu_0 H_{c2}$ is estimated from $0.9R_N$ and $\mu_0 H_{min}$ from $0.1R_N$. These values are extracted from R vs T curves (under perpendicular magnetic field, from 0 to 9 T, black symbols) and from R vs $\mu_0 H$ curves (under perpendicular magnetic field, from 0 to 20 T, grey symbols), I_{bias}= 0.1 μA. Data is fitted to a power law dependence. (b) Tilt-angle applied magnetic field dependence on $\mu_0 H_{c2}$ for nano-helix type 7. $\mu_0 H_{c2}$ values are extracted from R vs $\mu_0 H$ curves, I_{bias}= 0.1 μA.

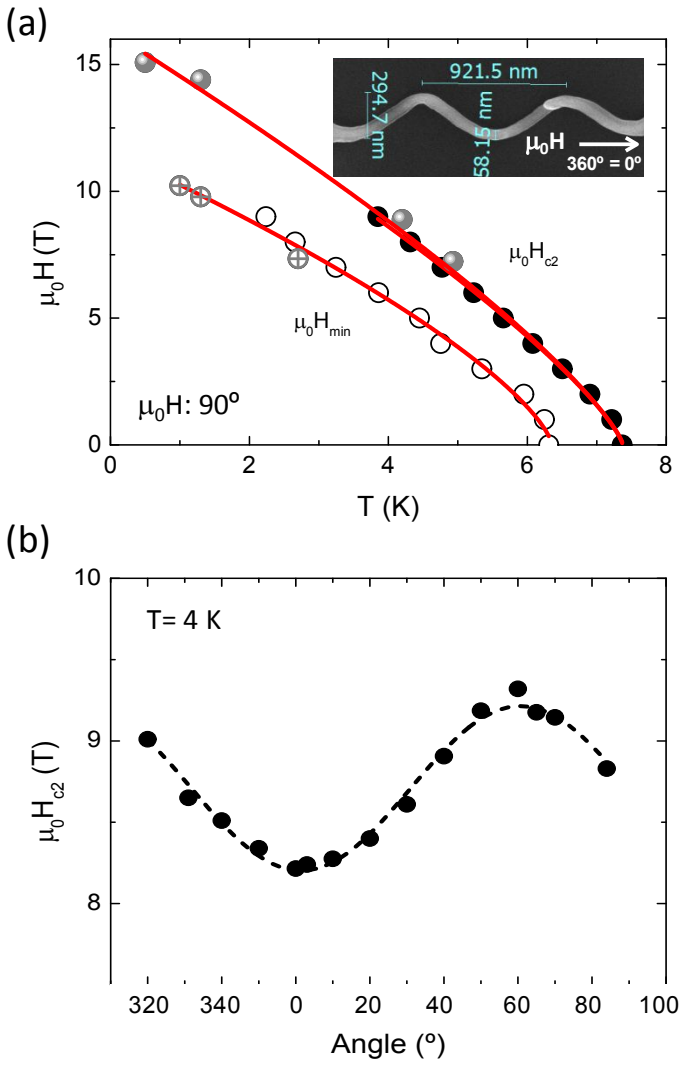

Figure 5. Experimental Resistance-vs-Current characteristics (left panels) for the nano-helix type 6, and simulated order parameter distributions plotted over the 2D surface of the helical structure (right panels) for the magnetic fields 1 T (upper – right panel) and 2 T (lower – right panel). The values of the applied transport current in units of the critical current are indicated in the panels. The critical currents are evaluated from the experimental data to be 3.3 μA for 1 T and 3.0 μA for 2 T. Different vortex and phase-slip patterns correspond to steps of resistance (the correspondence is shown by the arrows).

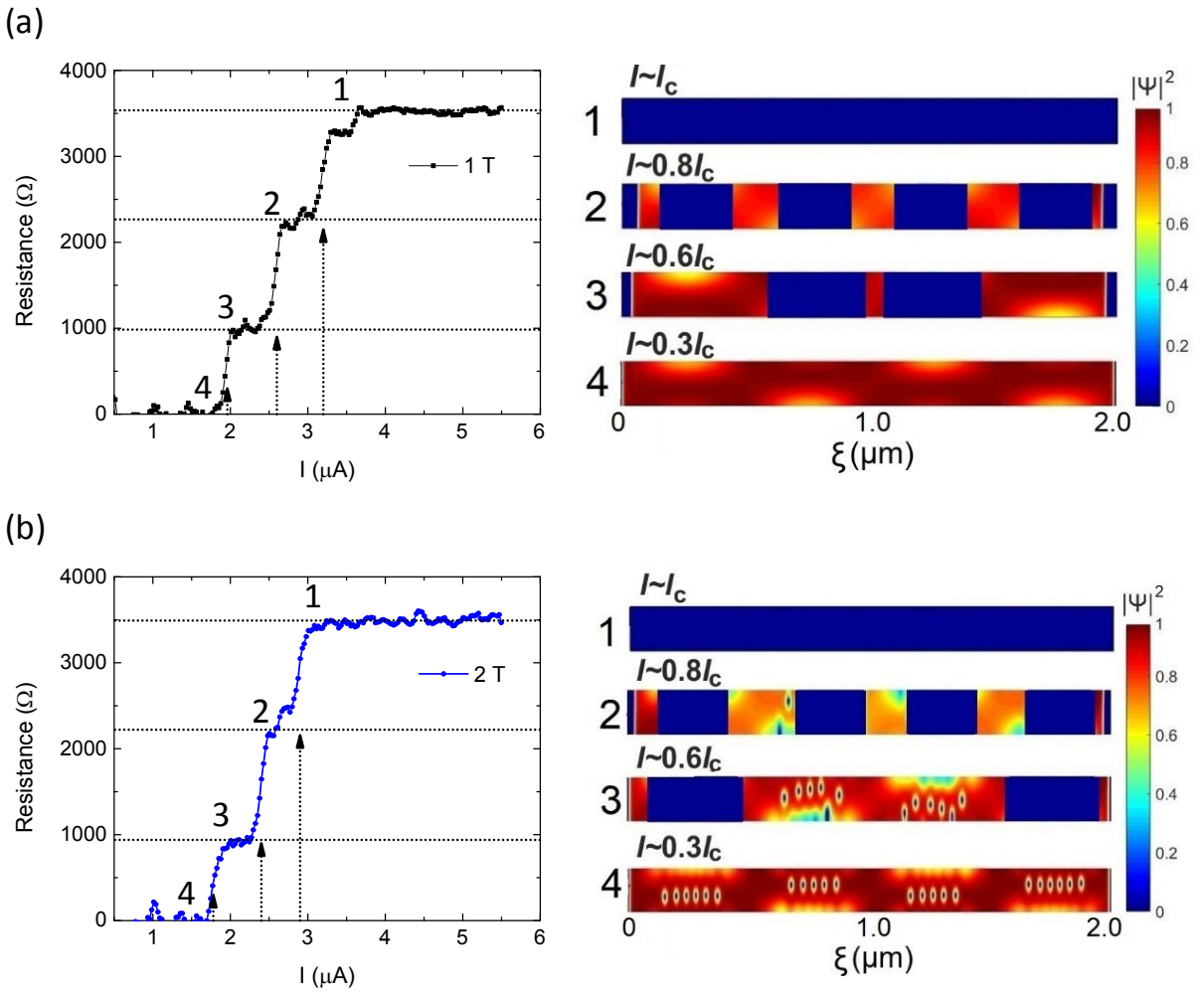

ASSOCIATED CONTENT

Supporting Information.

Methods: Growth of 3D helical nanostructures, nano-manipulation of 3D helical nanostructures, growth of auxiliary Pt FIBID nanocontacts, magnetotransport measurements, numerical simulations.

Movie of the elastic behavior and manipulation of the nano-helix.

The following files are available free of charge.

AUTHOR INFORMATION

Corresponding Author

* Address correspondence to Rosa Córdoba (rosa.cordoba.castillo@gmail.com) and José Mª De Teresa (deteresa@unizar.es).

ORCID

Rosa Córdoba: https://orcid.org/0000-0002-6180-8113

José María De Teresa: https://orcid.org/0000-0001-9566-0738

Dominique Mailly: https://orcid.org/0000-0002-2174-8785

Vladimir Fomin: https://orcid.org/0000-0002-8959-4831

Isabel Guillamón: https://orcid.org/0000-0002-2606-3355

Hermann Suderow: https://orcid.org/0000-0002-5902-1880

Author Contributions

R.C. and J.M.D.T. led the project and conceived the experiments. R.C. and D.M. grew the WC 3D nano-helices by using a He^+ microscope. R.C. made the auxiliary contacts to the nano-helices, measured their electrical transport behavior, performed the subsequent data analysis, and wrote the first version of the manuscript. O.G.S. and V.M.F. developed key conceptual ingredients for the interpretation. R.O.R. and E.I.S. performed numerical simulations. U. Z. and R. C. performed electrical transport experiments of nano-helices in tilted magnetic fields at the High Magnetic Field Laboratory in Nijmegen. I. G. and H. S. collaborated in the sample design and in the discussion of the results. All authors discussed the results, the manuscript, contributed to it, and have given approval to the final version of the manuscript.

Funding Sources

This work was supported by the financial support from Spanish Ministry of Economy and Competitiveness through the projects MAT2017-82970-C2-2-R, PIE201760E027, including FEDER funding, FIS2017-84330-R, MDM-2014-0377, EU ERC (Grant Agreement No. 679080), COST Grant No. CA16128 and STSM Grant 41199 for V.M.F. from COST Action CA16218, from the EU-H2020 research and innovation programme under grant agreement No 654360 NFFA-Europe, from regional Gobierno de Aragón (grants E13_17R) with European Social Fund (Construyendo Europa desde Aragón) and Comunidad de Madrid through project Nanofrontmag-CM (Grant No. S2013/MIT-2850). The French RENATECH network (French national nanofabrication platform). The support of the German Research Foundation (DFG) via Grant FO 956/5-1 is gratefully acknowledged. The computations were

performed on an HPC system at the Center for Information Services and High Performance Computing (ZIH) at TU Dresden.

ACKNOWLEDGMENT

This work was supported by the financial support from Spanish Ministry of Economy and Competitiveness through the projects and MAT2017-82970-C2-2-R, PIE201760E027, including FEDER funding, FIS2017-84330-R, MDM-2014-0377, EU ERC (Grant Agreement No. 679080), COST Grant No. CA16128 and STSM Grant 41199 for V.M.F. from COST Action CA16218, from the EU-H2020 research and innovation programme under grant agreement No 654360 NFFA-Europe, from regional Gobierno de Aragón (grants E13_17R) with European Social Fund (Construyendo Europa desde Aragón) and Comunidad de Madrid through project Nanofrontmag-CM (Grant No. S2013/MIT-2850). Authors acknowledge the LMA-INA for offering access to their instruments and expertise and the use of Servicio General de Apoyo a la Investigación-SAI, Universidad de Zaragoza, particularly the Servicio de Medidas Físicas. The support of the German Research Foundation (DFG) via Grant FO 956/5-1 is gratefully acknowledged. Authors acknowledge the Center for Information Services and High Performance Computing (ZIH) at TU Dresden for offering access to the HPC system. This work was supported by HFML-RU/NWO-I, member of the European Magnetic Field Laboratory (EMFL). It is part of the research program no. 132 "*High Field Magnet Laboratory: a global player in science in high magnetic fields*" financed by the Netherlands Organisation for Scientific Research (NWO).

REFERENCES

(1) Larbalestier, D. C.; Jiang, J.; Trociewitz, U. P.; Kametani, F.; Scheuerlein, C.; Dalban-Canassy, M.; Matras, M.; Chen, P.; Craig, N. C.; Lee, P. J.; Hellstrom, E. E. *Nat. Mater.* **2014**, *13* (4), 375–381.

(2) Reif, F. *Phys. Rev.* **1956**, *102* (5), 1417–1418.

(3) Bromberg, L.; Tekula, M.; El-Guebaly, L. .; Miller, R. *Fusion Eng. Des.* **2001**, *54* (2), 167–180.

(4) Schmuser, P. *Reports Prog. Phys.* **1991**, *54* (5), 683–730.

(5) Larbalestier, D.; Gurevich, A.; Feldmann, D. M.; Polyanskii, A. *Nature* **2001**, *414* (6861), 368–377.

(6) Barnes, P. N.; Sumption, M. D.; Rhoads, G. L. *Cryogenics (Guildf).* **2005**, *45* (10–11), 670–686.

(7) Tesche, C. D.; Clarke, J. *J. Low Temp. Phys.* **1977**, *29* (3–4), 301–331.

(8) Martinez, J.; Hijazi, Y.; Brzhezinskaya, M.; Bogozi, A.; Noel, J.; Vlasov, Y. A.; Larkins, G. L. *Phys. C Supercond.* **2007**, *466* (1–2), 101–105.

(9) Noel, J.; Hijazi, Y.; Martinez, J.; Vlasov, Y. A.; LarkinsJr, G. L. *Supercond. Sci. Technol.* **2003**, *16* (12), 1438–1441.

(10) Gutiérrez, J.; Llordés, A.; Gázquez, J.; Gibert, M.; Romà, N.; Ricart, S.; Pomar, A.; Sandiumenge, F.; Mestres, N.; Puig, T.; Obradors, X. *Nat. Mater.* **2007**, *6* (5), 367–373.

(11) Giordano, N. *Phys. Rev. Lett.* **1988**, *61* (18), 2137–2140.

(12) Fazio, R. *Phys. Rep.* **2001**, *355* (4), 235–334.

(13) Tonomura, A.; Kasai, H.; Kamimura, O.; Matsuda, T.; Harada, K.; Nakayama, Y.; Shimoyama, J.; Kishio, K.; Hanaguri, T.; Kitazawa, K.; Sasase, M.; Okayasu, S. *Nature* **2001**, *412* (6847), 620–622.

(14) Córdoba, R.; Baturina, T. I.; Sesé, J.; Yu Mironov, A.; De Teresa, J. M.; Ibarra, M. R.; Nasimov, D. A.; Gutakovskii, A. K.; Latyshev, A. V.; Guillamón, I.; Suderow, H.; Vieira, S.; Baklanov, M. R.; Palacios, J. J.; Vinokur, V. M. *Nat. Commun.* **2013**, *4* (1), 1437.

(15) Shulaker, M. M.; Hills, G.; Park, R. S.; Howe, R. T.; Saraswat, K.; Wong, H.-S. P.; Mitra, S. *Nature* **2017**, *547* (7661), 74–78.

(16) Lösch, S.; Alfonsov, A.; Dobrovolskiy, O. V.; Keil, R.; Engemaier, V.; Baunack, S.; Li, G.; Schmidt, O. G.; Bürger, D. *ACS Nano* **2019**, *13* (3), 2948–2955.

(17) Li, W.; Gu, C.; Warburton, P. A. *J. Nanosci. Nanotechnol.* **2010**, *10* (11), 7436–7438.

(18) Romans, E. J.; Osley, E. J.; Young, L.; Warburton, P. A.; Li, W. *Appl. Phys. Lett.* **2010**, *97* (22), 222506.

(19) Li, W.; Fenton, J. C.; Cui, A.; Wang, H.; Wang, Y.; Gu, C.; McComb, D. W.; Warburton, P. A. *Nanotechnology* **2012**, *23* (10), 105301.

(20) Córdoba, R.; Ibarra, A.; Mailly, D.; De Teresa, J. M. *Nano Lett.* **2018**, *18* (2), 1379–1386.

(21) Porrati, F.; Barth, S.; Sachser, R.; Dobrovolskiy, O. V.; Seybert, A.; Frangakis, A. S.; Huth, M. *ACS Nano* **2019**, acsnano.9b00059.

(22) Matsui, S.; Kaito, T.; Fujita, J.; Komuro, M.; Kanda, K.; Haruyama, Y. In *Papers from the 44th international conference on electron, ion, and photon beam technology and nanofabrication*; AVS: Rancho Mirage, California, (USA), 2000; Vol. 18, pp 3181–3184.

(23) Morita, T.; Kometani, R.; Watanabe, K.; Kanda, K.; Haruyama, Y.; Hoshino, T.; Kondo, K.; Kaito, T.; Ichihashi, T.; Fujita, J.; Ishida, M.; Ochiai, Y.; Tajima, T.; Matsui, S. *J. Vac. Sci. Technol. B Microelectron. Nanom. Struct.* **2003**, *21* (6), 2737.

(24) Esposito, M.; Tasco, V.; Todisco, F.; Benedetti, A.; Sanvitto, D.; Passaseo, A. *Adv. Opt. Mater.* **2014**, *2* (2), 154–161.

(25) Esposito, M.; Tasco, V.; Cuscunà, M.; Todisco, F.; Benedetti, A.; Tarantini, I.; Giorgi, M. De; Sanvitto, D.; Passaseo, A. *ACS Photonics* **2015**, *2* (1), 105–114.

(26) Fujii, T.; Iwasaki, K.; Munekane, M.; Takeuchi, T.; Hasuda, M.; Asahata, T.; Kiyohara, M.; Kogure, T.; Kijima, Y.; Kaito, T. *J. Micromechanics Microengineering* **2005**, *15* (10), S286–S291.

(27) Nakai, Y.; Kang, Y.; Okada, M.; Haruyama, Y.; Kanda, K.; Ichihashi, T.; Matsui, S. *Jpn. J. Appl. Phys.* **2010**, *49* (6), 06GH07.

(28) Scipioni, L.; Stern, L. A.; Notte, J.; Sijbrandij, S.; Griffin, B. *Adv. Mater. Process.* **2008**, *166* (6), 27.

(29) Maas, D.; van Veldhoven, E.; Chen, P.; Sidorkin, V.; Salemink, H.; van der Drift, E.; Alkemade, P. In *Metrology, Inspection, and Process Control for Microlithography Xxiv*; Raymond, C. J., Ed.; 2010; Vol. 7638.

(30) Alkemade, P. F. A.; Miro, H. *Appl. Phys. A* **2014**, *117* (4), 1727–1747.

(31) Kohama, K.; Iijima, T.; Hayashida, M.; Ogawa, S. *J. Vac. Sci. Technol. B Microelectron. Nanom. Struct.* **2013**, *31* (3), 031802.

(32) Guillamón, I.; Suderow, H.; Fernández-Pacheco, A.; Sesé, J.; Córdoba, R.; De Teresa, J. M.; Ibarra, M. R.; Vieira, S. *Nat. Phys.* **2009**, *5* (9).

(33) Makise, K.; Terai, H.; Tominari, Y.; Tanaka, S.; Shinozaki, B. *Sci. Rep.* **2016**, *6* (1), 27001.

(34) Gor ’kov, L. P. *J. Exptl. Theor. Phys.* **1959**, *36* (36), 1918–1923.

(35) Dinner, R. B.; Robinson, A. P.; Wimbush, S. C.; MacManus-Driscoll, J. L.; Blamire,

M. G. *Supercond. Sci. Technol.* **2011**, *24* (5), 055017.

(36) Basset, J.; Watfa, D.; Aiello, G.; Féchant, M.; Morvan, A.; Estève, J.; Gabelli, J.; Aprili, M.; Weil, R.; Kasumov, A.; Bouchiat, H.; Deblock, R. *Appl. Phys. Lett.* **2019**, *114* (10), 102601.

(37) Fomin, V. M.; Rezaev, R. O.; Levchenko, E. A.; Grimm, D.; Schmidt, O. G. *J. Phys. Condens. Matter* **2017**, *29* (39), 395301.

(38) Puig, T.; Rosseel, E.; Baert, M.; Van Bael, M. J.; Moshchalkov, V. V.; Bruynseraede, Y. *Appl. Phys. Lett.* **1997**, *70* (23), 3155–3157.

(39) Chiorescu, I.; Nakamura, Y.; Harmans, C. J. P. M.; Mooij, J. E. *Science* **2003**, *299* (5614), 1869–1871.

(40) Kadin, A. M.; Leung, M.; Smith, A. D. *Phys. Rev. Lett.* **1990**, *65* (25), 3193–3196.

(41) Dauler, E. A.; Kerman, A. J.; Rosenberg, D.; Pan, S.; Grein, M. E.; Molnar, R. J.; Correa, R. E.; Bawendi, M. G.; Berggren, K. K.; Moores, J. D.; Boroson, D. M. In *IEEE Photonic Society 24th Annual Meeting*; IEEE, 2011; pp 350–351.

(42) Natarajan, C. M.; Tanner, M. G.; Hadfield, R. H. *Supercond. Sci. Technol.* **2012**, *25* (6), 063001.

(43) Dubrovin, B. A.; Fomenko, A. T.; Novikov, S. P. *Modern Geometry -- Methods and Applications : Part I. The Geometry of Surfaces, Transformation Groups, and Fields*; Springer New York, 1984.